I···N Halogen bonding in 1:1 co-crystals formed between 1,4-diiodotetrafluorobenzene and the isomeric n-pyridinealdazines (n = 2, 3 and 4): Assessment of supramolecular association and influence upon solid-state photoluminescence properties†

Chien Ing Yeo,[a] Yee Seng Tan,[a] Huey Chong Kwong,[a] Vannajan Sanghiran Lee[b] and Edward R. T. Tiekink*[a]

a Research Centre for Crystalline Materials, School of Medical and Life Sciences, Sunway University, 47500 Bandar Sunway, Selangor Darul Ehsan, Malaysia

b Department of Chemistry, University of Malaya, 50603 Kuala Lumpur, Malaysia

E-mail: edwardt@sunway.edu.my (ERTT)

Abstract

1:1 Co-crystals formed between 1,4-diiodotetrafluorobenzene and each of the three isomeric **n**-pyridinealdazines (**n** = 2, 3 and 4) have been characterised by X-ray crystallography, a variety of spectroscopic methods, *viz*. IR, Raman, NMR: solution- and solid-state (^{13}C CP MAS and ^{13}C HPDEC MAS) and fluorescence as well as by computational chemistry techniques. The primary connection between the respective coformers arises from I···N halogen bonds which give rise to one-dimensional supramolecular chains of varying topology depending on the position of the nitrogen atom in the **n**-pyridinealdazine isomer. The energies calculated for the I···N contacts are relatively small, varying from -5.4 to -6.3 kcal/mol, with the maximum being in the crystal of the

n = 3 isomer. Notable in the molecular packing are C–I···π(pyridine) and C–F···π(arene) interactions in the crystals with the **3**- and **4**-pyridinealdazine coformers, respectively. The co-crystal formed by **2**-pyridinealdazine exhibited fluorescence emission.

Footnote

† Electronic supplementary information (ESI) available: Selected geometric parameters, Hirshfeld surface contacts, PXRD, IR, Raman and NMR (^{1}H, ^{13}C{^{1}H}, ^{15}N, ^{19}F and ^{127}I) spectra for **2**–**4**, and solid-state NMR spectra for **3** and **4** CCDC 2173827, 2173832 and 2173837 contain the supplementary crystallographic data for this paper. For ESI and crystallographic data in CIF or other electronic format see DOI: 10.1039/d0cexxxxxx

Introduction

The attractive interaction of a halogen atom with an electron-rich species such as a pyridine-nitrogen atom falls under the aegis of halogen bonding,[1] a phenomenon first appreciated crystallographically in crystals of the 1:1 multi-component crystal of Br_2 and dioxane which comprises supramolecular chains of alternating Br_2 and dioxane molecules featuring Br···O contacts;[2,3] related contacts were implicated experimentally prior to this solid-state result.[4,5] The apparent incongruity of having two like-charged species forming an attractive interaction has been resolved theoretically through the σ-hole concept whereby an electron-deficient region is apparent at the tip of the C–X bond, enabling the attractive interaction with an electron-rich region, such as afforded by a lone-pair of electrons.[6] The σ-hole concept has wide applicability[7,8] for related secondary bonding interactions,[9] a term that encompasses many supramolecular associations[10-13] based on σ-hole as well as the less common π-hole interactions.[14,15] The real breakthrough with

halogen bonding came with the appreciation that halogen bonds exhibit strength and directionality to rival conventional hydrogen bonding.[16-19] The strength of a halogen bond can be moderated by the nature of the halide as the σ-hole is at a maximum for the more polarizable iodide atom compared with its lighter congeners. The strength of the interaction is also sensitive to the nature of the substituents bound to the halide/local electronic environment as well as the basicity of nucleophile.[20,21]

With the above in mind, it is not surprising that a wide variety of aggregates[22] have been engineered within crystals[23] featuring iodide molecules. Up to (interpenetrated) three-dimensional aggregates featuring I···N halogen bonds have been described,[24] synthon polymorphism has been reported[25] and the utility of I···N halogen bonds for templating alkenes in positions suitable for solid-state [2 + 2] photocycloadditions also recently described.[26] A particularly noteworthy molecule in this context is 1,4-diiodotetrafluorobenzene (systematic name: 1,2,4,5-tetrafluoro-3,6-diiodobenzene), hereafter **1**, for which, owing to the presence of the four electronegative fluorides, the σ-hole effect is heightened for the iodide atoms. According to a search of the Cambridge Structural Database (CSD; version 5.42, two updates),[27] there are over 550 hits for crystals containing **1**. Naturally, not all of these structures refer to crystal engineering ambitions, but many do, in particular referring to the formation of I···N(pyridine) halogen bonds. Despite this intense interest, studies of **1** with the isomeric **n**-pyridinealdazine molecules, for **n** = 2, 3 and 4 (Fig. 1), have yet to be reported; hereafter these molecules are abbreviated as **n**-PyAld for **n** = 2, 3 and 4. Indeed, a search of the CSD shows no examples of I···N(pyridine) interactions involving **n**-PyAld molecules. This gap in knowledge reflects the general theme that **n**-PyAld are an understudied class of molecules. For example, while there are over 5,800 examples of the mainstay of

coordination polymer formation, 4,4'-bipyridine, bridging two metal centres, there are only 46, 112 and 238 examples of **2**-, **3**- and **4**-pyridinealdazines functioning in the same manner.

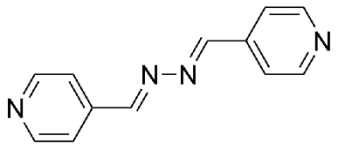

Fig. 1. Chemical diagram for **4**-pyridinealdazine (systematic name: 4-[(1E)-[(E)-2-(pyridin-4-ylmethylidene)hydrazin-1-ylidene]methyl]pyridine).

The lack of systematic investigation belies some rather interesting observations in the supramolecular chemistry of **n**-pyridinealdazines. For example, a recent study revealed four polymorphs of composition $\{Cd[S_2P(OMe)_2]_2(\mathbf{4}\text{-PyAld})\}_n$ including a scenario where metastable polymorphs could be captured by placing crystals directly into the liquid nitrogen cyrostream.[28] It is usual for **n**-pyridinealdazines, as with for other bipyridine-type molecules, to function as bridges in their metal complexes but exceptions occur. Thus, a monodentate mode of coordination is noted in $Zn[S_2CN(Me)CH_2CH_2OH)]_2(\mathbf{4}\text{-PyAld})$,[29] as well as in the bis adduct $Cd[S_2CN(Et)CH_2CH_2OH)]_2(\mathbf{4}\text{-PyAld})$,[30] and, most remarkably, in $\{Cd[S_2CN(i\text{-}Pr)CH_2CH_2OH)]_2(\mathbf{3}\text{-PyAld})\}_2$,[31] where the usually disrupted, upon complexation by bipyridine-type molecules,[32] binuclear $\{Cd[S_2CN(i\text{-}Pr)CH_2CH_2OH)]_2\}_2$ molecule is retained. The non-coordinating end of the **n**-PyAld molecules in the aforementioned crystals participate in hydroxyl-O–H···N(**n**-PyAld) hydrogen bonding instead, opening up the suggestion that the energies of stabilization afforded by coordinate (dative) bonds and conventional hydrogen bonding are in the same range.[33,34]

The isomeric **n**-pyridinealdazines have also afforded series of crystals enabling the evaluation of the influence of the isomeric form upon supramolecular aggregation, largely featuring carboxylic acid-O–H···N(pyridine) hydrogen bonding, such as in the co-crystal families formed with 2,2'-dithiobenzoic acid[35] and 4-nitrophenylacetic acid.[36] It was in this context that the title series of 1:1 co-crystals, **1**.**n**-PyAld were isolated. Herein, a detailed investigation of the supramolecular aggregation is described along with a correlation of the experimental structures with a range of spectroscopic techniques, for example, vibrational, solid-state NMR and fluorescence.

Experimental

Instrumentation

The melting points were determined on a Biobase automatic melting point apparatus MP450. The elemental analyses were performed on a Leco TruSpec Micro CHN Elemental Analyser. The powder X-ray diffraction (PXRD) patterns were measured on a Rigaku SmartLab Powder X-ray diffractometer with a capillary attachment using CuKα (λ = 1.5418 Å) radiation in the 2θ range 5 to 40°. The comparison between experimental and calculated (from CIFs) PXRD patterns was performed with Rigaku's PDXL2 software (https://www.rigaku.com/en/products/software/pdxl/overview). The IR spectra were measured on a Bruker Vertex 70v FTIR spectrophotometer equipped with a platinum ATR from 4000 to 400 cm^{-1} under vacuum conditions; abbreviations: s, strong; m, medium; w, weak, while the Raman spectra were measured on powdered samples on an Anton Paar Cora 5700 Raman instrument using laser power 300 mW and laser wavelength at 785 nm. The ^{1}H and $^{13}C\{^{1}H\}$ NMR spectra were

recorded in $CDCl_3$ solutions on a Bruker Ascend 400 MHz NMR spectrometer with chemical shifts relative to tetramethylsilane; abbreviations for NMR assignments: *s*, singlet; *d*, doublet; *dd*, doublet of doublets; *dt*, doublet of triplets; *dq*, doublet of quartets; *td*, triplet of doublet; *ddd*, doublet of doublet of doublets; *m*, multiplet; *br*, broad. The ^{15}N, ^{19}F and ^{127}I NMR spectra were recorded in $CDCl_3$ solution with chemical shifts relative to external reference: neat nitromethane coaxial $CDCl_3$ (^{15}N, 0 ppm), 0.05 % trifluorotoluene in $CDCl_3$ (^{19}F, -63.72 ppm) and 0.01 M potassium iodide in D_2O (^{127}I, 0 ppm), respectively. The solid-state NMR measurements were performed on a Bruker Ascend 400 MHz NMR spectrometer equipped with a PH MAS VTN 400SB BL4 N-P/H probe, operating at 100.623 MHz. The ground sample was packed in a 4 mm zirconia rotor with Kel-F cap. The $^{13}C\{^1H\}$ CP MAS (cross-polarization magic-angle spinning) and $^{13}C\{^1H\}$ HPDEC MAS (high power decoupling with magic-angle spinning) spectra were recorded at room-temperature with the SPINAL-64[37] pulse sequence at a spinning rate of 12 kHz, with ^{13}C chemical shift scales referenced to adamantane (38.48 ppm) as external standard. The $^{13}C\{^1H\}$ CP MAS spectra were performed with a $\pi/2$ pulse length of 4.6 μs and a contact time of 5 ms. The $^{13}C\{^1H\}$ HPDEC MAS spectrum was measured with a $\pi/2$ pulse length of 7.8 μs. All measurements were performed with recycle delays ranged from 5 to 35 s and a number of scans varied from 500 to 2000 until a reasonable signal-to-noise ratio was obtained. The luminescence spectra of solid samples were recorded on a JASCO FP-8600 spectrofluorometer equipped with liquid nitrogen cooled 100 mm ϕ integrating sphere. The low-temperature luminescent measurements were carried out on powdered samples immersed in a liquid nitrogen bath with constant flush of dried N_2.

Synthesis and characterisation

The chemicals and solvents used in this study, *i.e.* 1,4-diiodotetrafluorobenzene (Aldrich), the three isomeric **n**-pyridinecarbaldehydes, for n = 2, 3 and 4 (Acros Organic), hydrazine monohydrate (Merck), ethanol (Merck) and $CDCl_3$ (Merck) were used without further purification. The coformer **2**-PyAld was prepared in high yield (0.19 g, 91 %) by reacting **2**-pyridinecarbaldehyde (0.21 g, 2.0 mmol) and hydrazine monohydrate (0.05 g, 1.0 mmol) in ethanol following a literature procedure.[38] Using similar procedures, **3**-pyridinealdazine (0.19 g, 92 %) and **4**-PyAld (0.20 g, 94 %) were prepared. The preparation of **4** is described as a representative for that of **2** and **3**: **4**-PyAld (1 mmol, 0.21 g) in ethanol (20 ml) was added to an ethanol solution (30 ml) of 1,4-diiodotetrafluorobenzene (1 mmol, 0.40 g). The mixture was stirred for 30 mins at room-temperature followed by filtration. The filtrate was left for slow evaporation under ambient conditions, yielding yellow crystals after one week.

1

FTIR (cm^{-1}): 1456(s) ν(C–C), 939(s) ν(C–F), 757(m) ν(C–I). Raman (cm^{-1}): ν_{max} = 155, 414, 498, 638, 689, 1347, 1383, 1540, 1609. $^{13}C\{^1H\}$ NMR {$CDCl_3$}: δ 148.2–147.9 (*br*, m, CF), 145.7–145.4 (*br*, m, CI) ppm. ^{19}F NMR {$CDCl_3$}: δ -119.03 ppm. ^{127}I NMR {$CDCl_3$}: δ -17.2 ppm. ^{13}C SS NMR (100.623 MHz): δ 147.7 (*br*, CF), 78.4 (*br*, CI) ppm.

2

Yield: 0.49 g, 81 %. M. pt.: 441.2–442.1 K. Anal. Calcd. for $C_{18}H_{10}F_4I_2N_4$: C, 35.32; H, 1.65; N, 9.15%. Found: C, 35.17; H, 1.96; N, 8.81%. FTIR (cm^{-1}): 1626(m) ν(C=N), 1458(s) ν(C–C), 940(s) ν(C–F), 756(m) ν(C–I). Raman (cm^{-1}): ν_{max} = 151, 498, 994, 1010, 1225, 1296, 1383, 1437,

1561, 1570. ^{1}H NMR {$CDCl_3$}: δ 8.72 (*dq*, br, 2H, aryl-H_3, $^{3}J_{HH}$ = 4.83 Hz, $^{4}J_{HH}$ = 0.81 Hz), 8.68 (*s*, 2H, NCH), 8.13 (*dt*, 2H, aryl-H_6, $^{3}J_{HH}$ = 7.88 Hz, $^{4}J_{HH}$ = 0.99 Hz), 7.80 (*td*, 2H, aryl-H_5, $^{3}J_{HH}$ = 7.73 Hz, $^{4}J_{HH}$ = 1.62 Hz), 7.38 (*ddd*, 2H, aryl-H_4, $^{3}J_{HH}$ = 7.52 Hz, $^{4}J_{HH}$ = 4.86 Hz, $^{5}J_{HH}$ = 1.13 Hz) ppm. $^{13}C\{^{1}H\}$ NMR {$CDCl_3$}: δ 162.3 (NCH), 153.0 (aryl-C_1), 150.2 (aryl-C_3), 148.2–147.9 (*br*, m, CF), 145.7–145.4 (*br*, m, CI), 136.8 (aryl-C_5), 125.3 (aryl-C_4), 122.7 (aryl-C_6) ppm. ^{15}N NMR {$CDCl_3$}: δ 0.0 ppm. ^{19}F NMR {$CDCl_3$}: δ -119.06 ppm. ^{127}I NMR {$CDCl_3$}: δ -19.4 ppm. ^{13}C SS NMR: δ 164.8 (NCH), 151.6 (overlapped, aryl-$C_{1,3}$), 147.6–146.3 (*br*, m, CF), 139.7 (aryl-C_5), 126.3 (aryl-C_4), 122.0 (aryl-C_6), 78.9 (*br*, CI) ppm.

3

Yield: 0.48 g, 79 %. M. pt.: 443.2–443.8 K. Anal. Calcd. for $C_{18}H_{10}F_4I_2N_4$: C, 35.32; H, 1.65; N, 9.15%. Found: C, 35.31; H, 1.90; N, 8.98%. FTIR (cm^{-1}): 1625(m) ν(C=N), 1456(s) ν(C–C), 938(s) ν(C–F), 753(m) ν(C–I). Raman (cm^{-1}): ν_{max} = 153, 498, 1005, 1026, 1228, 1417, 1552, 1588. ^{1}H NMR {$CDCl_3$}: δ 8.98 (*d*, 2H, aryl-H_2, $^{4}J_{HH}$ = 1.80 Hz), 8.70 (*dd*, 2H, aryl-H_4, $^{3}J_{HH}$ = 4.81 Hz, $^{4}J_{HH}$ = 1.62 Hz), 8.68 (*s*, 2H, NCH), 8.22 (*dt*, 2H, aryl-H_6, $^{3}J_{HH}$ = 7.94 Hz, $^{5}J_{HH}$ = 1.82 Hz), 7.40 (*dd*, 2H, aryl-H_5, $^{3}J_{HH}$ = 7.90 Hz, $^{4}J_{HH}$ = 4.83 Hz) ppm. $^{13}C\{^{1}H\}$ NMR {$CDCl_3$}: δ 160.0 (NCH), 152.3 (aryl-C_4), 150.7 (aryl-C_2), 148.2–147.9 (*br*, m, CF), 145.7–145.4 (*br*, m, CI), 135.0 (aryl-C_6), 129.9 (aryl-C_1), 124.0 (aryl-C_5) ppm. ^{15}N NMR {$CDCl_3$}: δ 0.0 ppm. ^{19}F NMR {$CDCl_3$}: δ -119.07 ppm. ^{127}I NMR {$CDCl_3$}: δ -36.3 ppm. ^{13}C SS NMR: δ 160.5 (NCH), 151.9 (overlapped, aryl-$C_{2,4}$), 148.9–145.4 (*br*, m, CF), 135.5 (aryl-C_6), 131.6 (aryl-C_1), 126.0 (aryl-C_5), 80.4 (*br*, CI) ppm.

4

Yield: 0.52 g, 85 %. M. pt.: 473.0–474.0 K. Anal. Calcd. for $C_{18}H_{10}F_4I_2N_4$: C, 35.32; H, 1.65; N, 9.15%. Found: C, 35.25; H, 1.68; N, 8.83%. FTIR (cm^{-1}): 1628(w) ν(C=N), 1454(s) ν(C–C), 938(s) ν(C–F), 755(m) ν(C–I). Raman (cm^{-1}): ν_{max} = 151, 498, 996, 1205, 1240, 1326, 1538, 1584. ^1H NMR {$CDCl_3$}: δ 8.75 (*dd*, 4H, aryl-$H_{3,5}$, $^3J_{HH}$ = 4.56 Hz, $^4J_{HH}$ = 1.40 Hz), 8.57 (*s*, 2H, NCH), 7.70 (*dd*, 4H, aryl-$H_{2,6}$, $^3J_{HH}$ = 4.56 Hz, $^4J_{HH}$ = 1.41 Hz) ppm. $^{13}C\{^1H\}$ NMR {$CDCl_3$}: δ 160.7 (NCH), 150.8 (aryl-$C_{3,5}$), 148.2–147.9 (*br*, m, CF), 145.7–145.4 (*br*, m, CI), 140.8 (C_1), 122.3 (aryl-$C_{2,6}$) ppm. ^{15}N NMR {$CDCl_3$}: δ 0.0 ppm. ^{19}F NMR {$CDCl_3$}: δ -119.07 ppm. ^{127}I NMR {$CDCl_3$}: δ -23.3 ppm. ^{13}C SS NMR: δ 163.8 (NCH), 149.3–148.0 (*br*, overlapped, aryl-$C_{3,5}$ and CF), 143.6 (aryl-C_1), 125.2, 123.5 (aryl-$C_{2,6}$), 81.8 (*br*, CI) ppm.

X-ray crystallography

Intensity data for **2–4** were measured at 100 K on a Rigaku/Oxford Diffraction XtaLAB Synergy diffractometer (Dualflex, AtlasS2) fitted with CuKα radiation (λ = 1.54178 Å). Data processing and absorption corrections (Gaussian) were accomplished with CrysAlis Pro.[39] The structures were solved by direct methods.[40] Full-matrix least-squares refinement on F^2 with anisotropic displacement parameters for all non-hydrogen atoms was performed.[41] The C-bound H atoms were placed on stereochemical grounds and refined with fixed geometries. Towards the end of each refinement, a weighting scheme of the form $w = 1/[\sigma^2(F_o^2) + (aP)^2 + bP]$ where $P = (F_o^2 + 2F_c^2)/3$ was introduced. In the refinement of **4**, two reflections, *i.e.* (1 5 10) and (-1 5 6), were omitted from the final cycles of refinement owing to poor agreement. The maximum residual electron density peaks were located in the vicinity of the iodide atoms. The programs WinGX,[42]

ORTEP-3 for Windows,[42] PLATON[43] and DIAMOND[44] were also used in the study. Crystal data and refinement data are presented in Table 1.

Table 1 Crystal data and refinement details for co-crystals **2**–**4** [a]

Co-crystal	**2**	**3**	**4**
Crystal size/mm^3	0.14 × 0.18 × 0.18	0.08 × 0.11 × 0.20	0.06 × 0.10 × 0.32
Space group	$P2_1/c$	$P2_1/c$	$I2/a$
a/Å	8.19820(11)	10.84010(11)	24.5350(4)
b/Å	9.94832(12)	7.44774(7)	4.12409(7)
c/Å	11.70649(14)	11.95687(12)	38.7414(6)
β/°	91.4133(12)	100.6098(10)	107.1887(17)
V/Å^3	954.47(2)	948.826(16)	3744.95(10)
Z	2	2	8
D_c/g cm^{-3}	2.130	2.142	2.171
λ(CuKα)/mm^{-1}	26.341	26.498	26.854
Measured data	11930	12110	23058
θ range/°	5.4–75.2	4.2–75.2	3.8–75.3
Unique data	1964	1958	3857
Observed data ($I \geq 2.0\sigma(I)$)	1961	1937	3811
No. parameters	127	127	253
R, obs. data; all data	0.032; 0.032	0.025; 0.025	0.033; 0.033
a; b in weighting scheme	0.056; 1.493	0.043; 0.886	0.064; 7.215
R_w, obs. data; all data	0.083; 0.083	0.066; 0.066	0.090; 0.090

Range of residual electron density peaks/eÅ^{-3}	-2.77–0.61	-0.91–0.70	-2.29–0.92

[a] Data common to all co-crystals analysed at 100 K: formula: $C_{12}H_{10}N_4$, $C_6F_4I_2$; formula weight: 612.10; crystal system: monoclinic; crystal colour: yellow.

Computational studies

Most of the calculations were performed using Gaussian 09[45] at the M062X/def2-tzvp[46-48] level appropriate for halogen-bonded systems[49] with the basis set obtained from Basis Set Exchange site.[50] The calculations were carried out on optimised molecules of **1**, **n**-PyAld (**n** = 2, 3 and 4) while single-point calculations were performed for co-crystals **2–4**. The molecular electrostatic potential surfaces (MEP) were mapped with an isovalue of 0.001 a.u. and rendered between −0.015 and +0.015 a.u. The quantitative analysis of the molecular surfaces was performed with Multiwfn.[51] The same level of theory was used to calculate the interaction energies using the geometries of the reactants extracted from the crystal structures with corrections for the basis set superposition error (BSSE) employing the Boys–Bernardi counterpoise technique.[52] The emission properties of **1** was predicted using the TD-DFT method based on the S_0 and S_1 optimised geometries at the B3LYP level of theory,[53-55] using 6-311++G(*d*,*p*) basis set for C, H, N, F atoms and LANL2DZ basis set for I.

Results and discussion

Synthesis

Three isomeric 1:1 co-crystals **2–4** have been isolated as yellow crystals from the 1:1 co-crystallisation from ethanol of 1,4-diodotetrafluorophenyl (**1**) and each **n**-PyAld isomer. The co-

crystals were characterised by X-ray crystallography and a range of spectroscopic and computational chemistry techniques. The X-ray powder diffraction patterns for **2–4** (ESI† Fig. S1) overlay those calculated from the CIFs indicating the bulk material matches the results obtained from the respective single crystal X-ray diffraction measurement.

X-ray crystal structures

The molecular structures of co-crystals **2–4** are shown in Fig. 2. The crystallographic asymmetric-unit of **2** comprises half a molecule of **1**, as this is disposed about a centre of inversion, as well as half a molecule of **2**-PyAld which is also disposed about a centre of inversion. A similar situation pertains in **3**. In **4**, coformer **1** occupies a general position and there are two half molecules of **4**-PyAld, each disposed about a centre of inversion, to give the 1:1 stoichiometry of **2** and **3**.

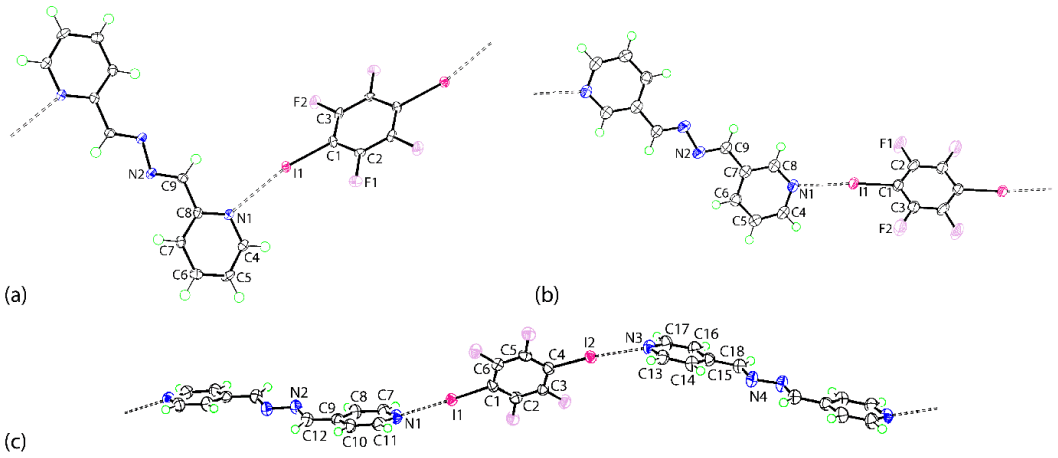

Fig. 2. Molecular structures of the constituents of co-crystals **2–4**: (a) **2** (the full molecule of **1** is generated by the application of symmetry operation 2-*x*, -*y*, 2-*z* and for **2**-PyAld by 1-*x*, 1-*y*, 1-*z*), (b) **3** (**1**: 1-*x*, -*y*, 2-*z* and **3**-PyAld: -1-*x*, -*y*, 1-*z*) and (c) **4** (**4**-PyAld-N1: -½-x, -½-y, ½-z and **4**-PyAld-N3: 1-*x*, 1-*y*, -*z*), showing atom labelling schemes and displacement parameters at the 70% probability level.

Selected geometric parameters for **2–4** are collated in ESI† Table S1 and show no systematic variations in the key C–I, C–N and N–N bond lengths, nor in the C–C–I, C–N–C and C–N–N bond angles. By contrast, variations depending on the isomeric form are noted for the I···N separations. Thus, the I···N separation increases in the order **4** (2.811(3) & 2.836(3) Å) < **3** (2.856(2) Å) < **2** (2.927(3) Å).

A search of the CSD[27] indicated a total of 965 all-organic crystals with at least one I···N halogen bond equal to or less than the sum of the van der Waals radii; ions were excluded from the search. This returned 813 hits with 1254 independent I···N distances. The average and mean I···N distances computed to 2.918 and 2.879 Å, respectively. Given the temperature dependence of weak interactions, a second search was performed with the restriction that the temperature of the experiment was 100 K, as in the present investigation. This search yielded 131 hits and 218 independent I···N distances. The average and mean values for I···N in the second search contracted to 2.898 and 2.851 Å, respectively. A more refined search was performed whereby the I atom was constrained to be part of **1**. At all temperatures, there were 193 hits with the average and median I···N distances being 2.924 and 2.869 Å, respectively. When the additional 100 K restriction was applied, the average and median I···N distances decreased to 2.914 and 2.844 Å, respectively. Based on these results, the I···N distance in **2** may be considered longer than usual, that in **3** conforming to the median value and the distances for **4** being comparable and marginally shorter than the median value.

Among all structures determined at 100 K, the shortest I···N distance, *i.e.* 2.477(4) Å, involves a I atom of I_2 and a pyridine-N of (*E*)-1,2-bis(pyridine-4-yl)diazene.[56] The longest separation was noted for a **1**-I···N(1,10-phenanthroline) contact, *i.e.* 3.488(9) Å, for a bifurcated

iodide atom; it is noted there are several shorter I···N contacts in this co-crystal in addition to this long contact.[57] These data are complemented by high resolution X-ray data enabling experimental charge density studies of short as well as relatively long I···N interactions. In the case of the former, a I···N separation of 2.6622(4) Å was found in the 1:2 co-crystal formed between **1** and 4-(dimethylamino)pyridine, a centrosymmetric three-molecule aggregate.[58] A large electron density of 0.359(5) e·Å^{-3} is noted in the critical point of the I···N interaction. In the case of a longer I···N interaction,[59] as in the two-molecule aggregate formed by iodobenzene and quinuclidine, the I···N separation of 2.9301(4) Å shows a significantly reduced electron density of 0.186(4) e·Å^{-3} for the bond critical point.

The supramolecular chains sustained by the I···N halogen bonds in **2–4** are illustrated in Fig. 3; the chain in **4** comprises both independent **4**-PyAld molecules. The chains are oriented along [1 -1 1], [2 0 1] and [3 3 -1], respectively. While there is a distinct step topology for the chain in **2**, which correlates with the 2-position of the pyridine-nitrogen atom, discernible flattening of the chains in **3** and, especially, **4**, is noted for which the topology is better described as undulating. These observations correlate with the pitch of the chains, defined as the distance between translationally related iodide atoms, which increase in the order **2** (17.2768(3) Å) < **3** (22.7495(4) Å) < **4** (23.2928(10) & 23.6037(10) Å). In turn, the pitches correlate with the span of the nitrogen donors, 8.072(4), 10.704(3) and 11.362(5) & 11.403(5) Å, for **2–4**, respectively.

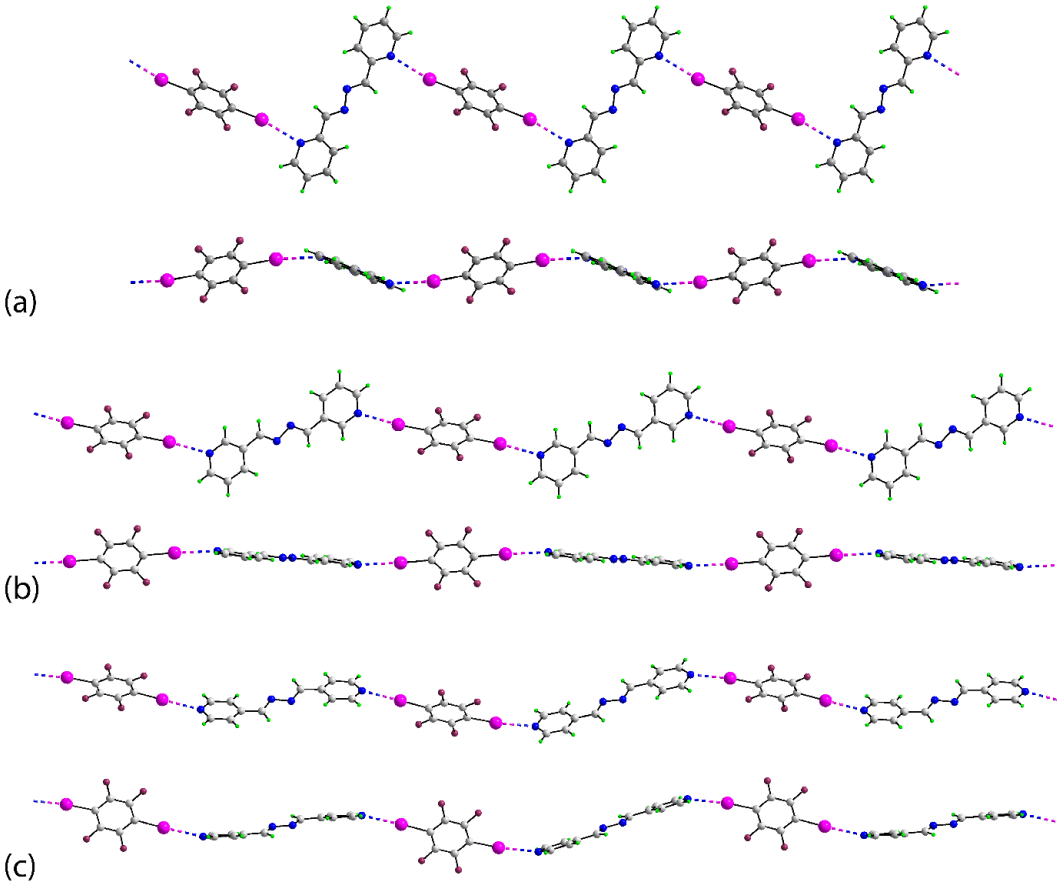

Fig. 3. Two views of the supramolecular chains in co-crystals (a) **2**, (b) **3** and (c) **4**.

The first analysis of the molecular packing in the crystals of **2–4** is based on the geometric criteria assumed in PLATON;[43] geometric parameters characterising the intermolecular connectivity are given in Table 2. The molecular packing in **2** comprises layers of chains with connections between successive chains being of the type π(pyridine)···π(pyridine). The layers stack in an ···ABAB··· fashion along the *c*-axis with the primary connections between layers being pyridine-C–H···F interactions. A view of the unit-cell contents is shown in Fig. 4(a).

Table 3. Summary of intermolecular interactions (A–H···B; Å, º) operating in the crystals of **2**–**4**

A	H	B	H···B	A···B	A–H···B	Symmetry
	operation					
2						
Cg(N1,C4-C8)	–	Cg(N1,C4-C8)	–	3.8273(19)	0[a]	1-*x*, -*y*, 1-*z*
C4	H4	F2	2.58	3.366(4)	140	2-*x*, -½+*y*, 1½-*z*
C5	H5	F1	2.62	3.428(4)	143	*x*, -½-*y*, -½+*z*
3						
Cg(N1,C4-C8)	–	Cg(N1,C4-C8)	–	3.8472(17)	0[a]	-*x*, -*y*, 1-*z*
C9	H9	F2	2.59	3.400(4)	144	-1+*x*, *y*, *z*
C4	H4	F1	2.48	3.422(4)	172	*x*, ½-*y*, -½+*z*
C1	I1	Cg(N1,C4-C8)	3.6369(12)	4.062(3)	85.81(8)	-*x*, -½+*y*, 1½-*z*
4						
Cg(N1,C7-C11)	–	Cg(N1,C7-C11)	–	4.124(2)	0[a]	*x*, 1+*y*, *z*
Cg(N3,C13-C17)	–	Cg(N3,C13-C17)	–	4.124(2)	0[a]	*x*, 1+*y*, +*z*
C2	F1	Cg(C1-C6)	3.489(3)	3.577(4)	82.7(2)	*x*, -1+*y*, +*z*

C5	F3	Cg(C1-C6)	3.489(3)	3.574(4)	82.63(19)	*x*, 1+*y*, +*z*
C8	H8	F3	2.62	3.529(4)	160	-½+*x*, 1-*y*, *z*
C16	H16	F2	2.55	3.393(5)	148	½-*x*, 1+*y*, -*z*
C18	H18	F2	2.51	3.369(4)	150	½-*x*, 1+*y*, -*z*

a angle between pyridine rings

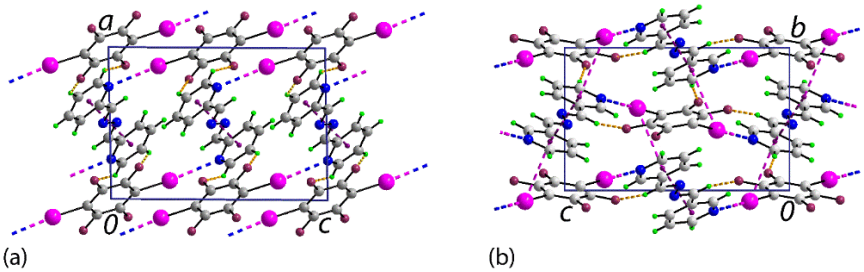

Fig. 4. Unit-cell diagrams for (a) **2** and (b) **3** with views in projection down the *b*-axis and *a*-axis, respectively. The π···π, C–H···F and C–I···π(pyridine) interactions are shown as purple, orange and pink dashed lines, respectively.

To a first approximation, the packing in **3** resembles that in **2**. Layers in the *ac*-plane stack along the *b*-axis in an ···ABAB··· fashion; the connection between chains are of the type π(pyridine)···π(pyridine) with supporting imine-C–H···F interactions. Pyridine-C–H···F contacts feature between layers as do side-on C–I···π(pyridine) interactions. A review appeared recently of C–I···π(arene) interactions.[60] The side-on approach of the iodide atom to the pyridine ring is indicative of an I(lone-pair)···π interaction as opposed to a σ-hole interaction, with the latter being significantly more prevalent; Fig. 4(b) shows a view of the unit-cell contents.

While the π(pyridine)···π(pyridine) interactions persist in the packing of **4**, important contributing interactions to the supramolecular layer are of the type parallel C–F···π(arene), Fig. 5(a). The connections between layers, that stack along the *c*-axis, are pyridine-C–H···F and imine-C–H···F contacts involving the same bifurcated F2 atom. A view of the unit-cell contents is shown in Fig. 5(b).

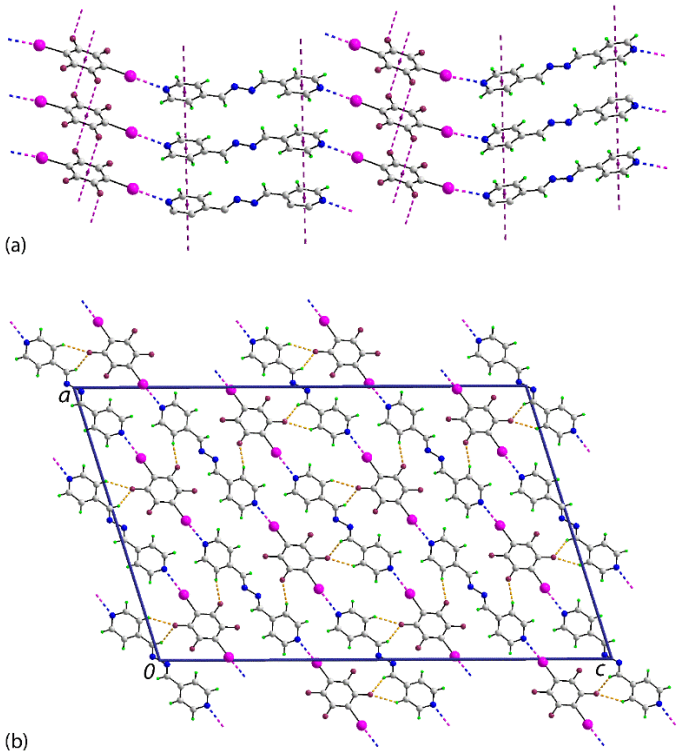

Fig. 5. Unit-cell diagrams for **4**: (a) the supramolecular layer featuring C–F···π(arene) and π(pyridine)···π(pyridine) interactions, and (b) a view in projection down the *b*-axis highlighting the bifurcated C–H···F interactions. The π···π, C–H···F and C–F···π(arene) interactions are shown as purple, orange and pink dashed lines, respectively.

The role of fluoride in supramolecular association is open to on-going debate[61-64] and reflecting this and in order to gain a further appreciation of the supramolecular association in **2–4**, a thorough analysis of the calculated Hirshfeld surfaces was undertaken (see below).

Finally, systematic trends are apparent in the values of density and packing efficiency. Thus, the calculation crystal densities increase from **2** to **4**, *i.e.* 2.130, 2.142 and 2.171 g cm^{-3}, respectively, which correlate with the trend in packing efficiency,[43] *i.e.* 69.9, 70.3 and 71.3%, respectively.

Hirshfeld surface analysis

Molecular Hirshfeld surface analysis and two-dimensional fingerprint plots for **2–4** were obtained using *CrystalExplorer 17*.[65] Hirshfeld surfaces were generated using very high surface resolution[66] employing TONTO.[67] The d_{norm}-plots were mapped with a colour scale between -0.347 a.u. (blue) and 0.971 a.u. (red). The identified contacts from this analysis are summarised in Table 3.

Table 3. Summary of short interatomic contacts (Å) identified from the calculated Hirshfeld surfaces of **2**–**4** [a]

Contact	Distance	Symmetry operation
2		
I1···N1	2.93	*x*, *y*, *z*
C4–H4···F2	2.48	2-*x*, -½+*y*, 1½-*z*
C5–H5···F1	2.52	*x*, -½-*y*, -½+*z*
C6–H6···N2	2.60	1-*x*, -½+*y*, ½-*z*
C1–I1···Cg(N1/C4-C8)	4.02	*x*, ½-*y*, ½+*z*
3		
I1···N1	2.86	*x*, *y*, *z*
C4–H4···F1	2.35	*x*, ½-*y*, -½+*z*
C6–H6···F2	2.77	-*x*, -*y*, 1-*z*
C9–H9···F2	2.48	-*x*, -*y*, 1-*z*
C1–I1···Cg(N1/C4-C8)	3.64	-*x*, -½+*y*, 1½-*z*
4		
I1···N1	2.81	*x*, *y*, *z*
I2···N3	2.84	*x*, *y*, *z*

C8–H8···F3	2.50	-½+*x*, 1-*y*, *z*
C12···F4	2.91	-*x*, -1½+*y*, ½-*z*
C16–H16···F2	2.44	½-*x*, 1+*y*, -*z*
C18–H18···F2	2.40	½-*x*, 1+*y*, -*z*
C2–F1···Cg(C1-C6)	3.49	*x*, -1+*y*, *z*
C5–F3···Cg(C1-C6)	3.49	*x*, 1+*y*, *z*

a The interatomic distances were measured in *CrystalExplorer17* where the X—H bond lengths have been adjusted to their neutron values

The d_{norm}-mapped Hirshfeld surfaces on the **n**-PyAld molecules feature bright-red spot near the pyridine-N atoms reflecting the I···N halogen bonds, Fig. 6.

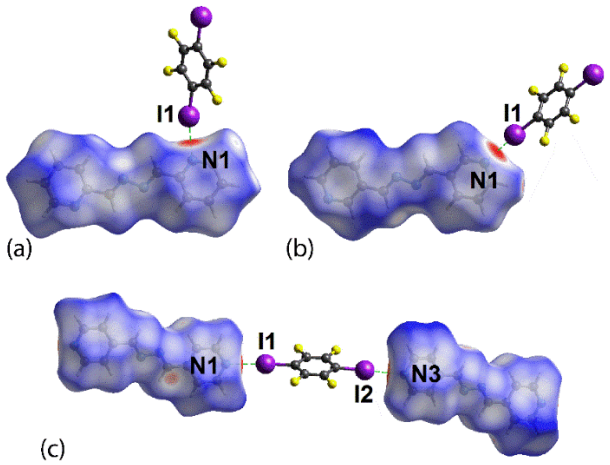

Fig. 6. Views of the d_{norm}-mapped Hirshfeld surfaces highlighting the intense red spots arising from the I···N halogen bonds for (a) **2** (b) **3** and (c) **4**.

The majority of the faint red spots near the pyridine- and imine-H atoms correspond to C–H···F contacts in **2**, **3** and **4** (Fig. 7). In addition, the weak pyridine–C6–H6···N2(hydrazine)

and imine-C12···F4 contacts are observed in the d_{norm}-mapped Hirshfeld surface of **2**-PyAld, Fig. 7(a), and **4**-PyAld, Fig. 7(c), respectively.

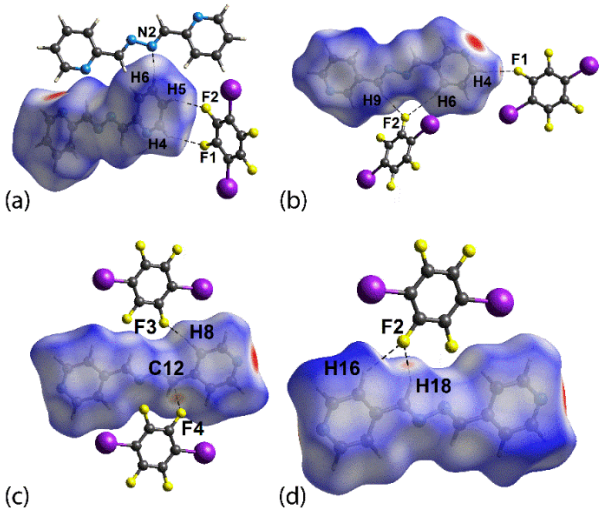

Fig. 7. Views of the d_{norm}-mapped Hirshfeld surfaces highlighting the C–H···F, C–H···N and C···F interactions in (a) **2**, (b) **3** (c) **4**.

Even though the halide···π interactions were not manifested on the d_{norm}-mapped Hirshfeld surfaces, these are reflected as a distinctive orange 'pothole' on the shape-index-mapped Hirshfeld surfaces of Fig. 8. In the crystals of **2** and **3**, the I···π interactions are evinced on the surfaces of the **2**-PyAld and **3**-PyAld molecules in Fig. 8(a) and (b), respectively, and the F···π interactions in the crystal of **4** are shown on the shape-index-mapped Hirshfeld surface of **1**.

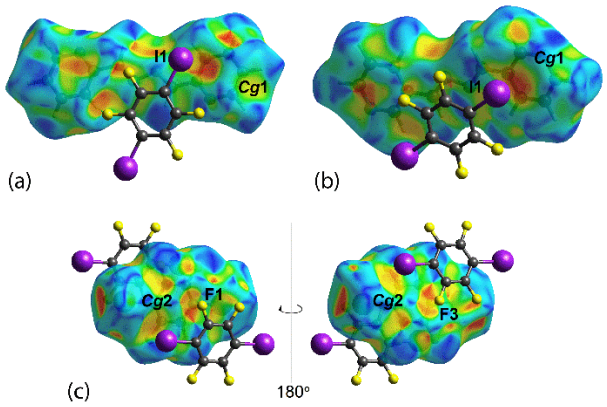

Fig. 8. Views of the shape-index-mapped Hirshfeld surfaces highlighting the halide···π interactions (a) **2**, (b) **3** and (c) **4**.

Finally, the long-range π···π interactions between the pyridine rings in the crystals of **2** and **3** are observed through the curvedness-mapped Hirshfeld surface of the individual **n**-PyAld molecules, Fig. 9.

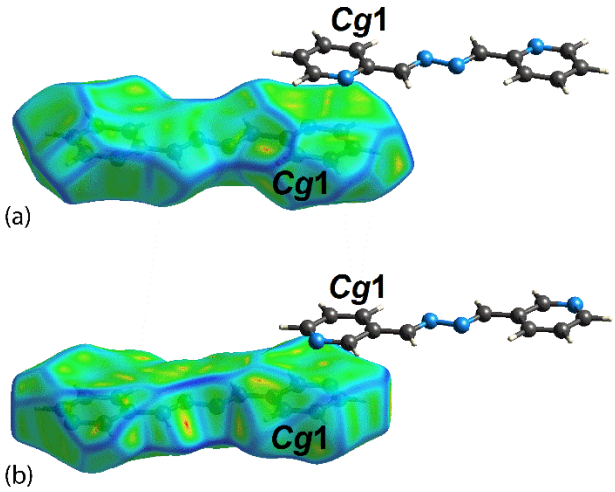

Fig. 9. Views of the curvedness-mapped Hirshfeld surfaces showing the long-range π···π interactions for (a) **2** and (b) **3**.

The percentage contributions of interatomic contacts to the Hirshfeld surfaces of overall **2**–**4**, individual molecules of **1** and each of **n**-PyAld in **2**–**4** are collected in ESI† Table S2.

Notable trends are evident reflecting the different identified contacts in the molecular packing. For example, reflecting the diminishing importance of C–I···π interactions in **4** *cf*. **2** and **3**, the contributions of C···I/I···C to the overall Hirshfeld surface decreases from **2** to **4**, *i.e*. 6.1, 5.8 and 2.0%, respectively. Conversely, reflecting the increasing importance of C–F···π interactions in **4** *cf*. **2** and **3**, the contributions of C···F/F···C increase, *i.e*. 1.9, 3.2 and 6.2%, for **2** to **4**, respectively. The greatest contributions to the overall surfaces for **2–4** are from F···H/H···F contacts, being 24.6, 26.9 and 23.9%, respectively.

Molecular electrostatic potentials (MEP)

To gain insight of the role of **1** and **n**-PyAld in I···N halogen bond formation as a prelude to the spectroscopic analysis, the MEP surfaces of the optimised structures of **1** and **n**-PyAld (**n** = 2, 3 and 4) and of the experimental co-crystals **2–4** (single point) were calculated, in accord with literature precedents,[68,69] with the results presented in Table 4.

Table 5. Summary of $V_{s,max}$, $V_{s,min}$, ΔV_s (a.u.) and energies (kcal/mol) for **1**, **n**-PyAld and **2**–**4**

Compound	$\mathbf{V_{s,max}}$	$\mathbf{V_{s,min}}$	$\mathbf{\Delta V_s}$	**ΔE**
1	0.051 (32.1)	–	–	–
2-PyAld	–	−0.049 (−31.0)	–	–
3-PyAld	–	−0.052 (−32.8)	–	–
4-PyAld	–	−0.053 (−33.4)	–	–
2	0.051 (32.1)	−0.049 (−31.0)	0.100 (63.1)	−0.0086 (−5.4)
3	0.051 (32.1)	−0.052 (−32.8)	0.103 (64.9)	−0.0100 (−6.3)
4	0.051 (32.1)	−0.053 (−33.4)	0.104 (65.5)	−0.0096 (−6.0) [a]

			−0.0093 (−5.8) [b]

[a]I1···N1 and [b]I2···N3.

The calculated MEP surface of optimised **1** shows the presence of σ- and π-holes, reflecting its ability to function as a ditopic halogen bond donor, Fig. 10. In **1**, the positive region at the σ-hole showed the greatest potential ($V_{s,max}$) *cf.* with the π-hole.[70] The presence of the σ-hole in **1** is complemented by the electrostatically negative (red) region in each optimised **n**-PyAld molecule. The minimum negative potentials ($V_{s,min}$) are located near the pyridine-N atoms, implying their greater potential to participate in halogen bond formation *cf.* imine-N.

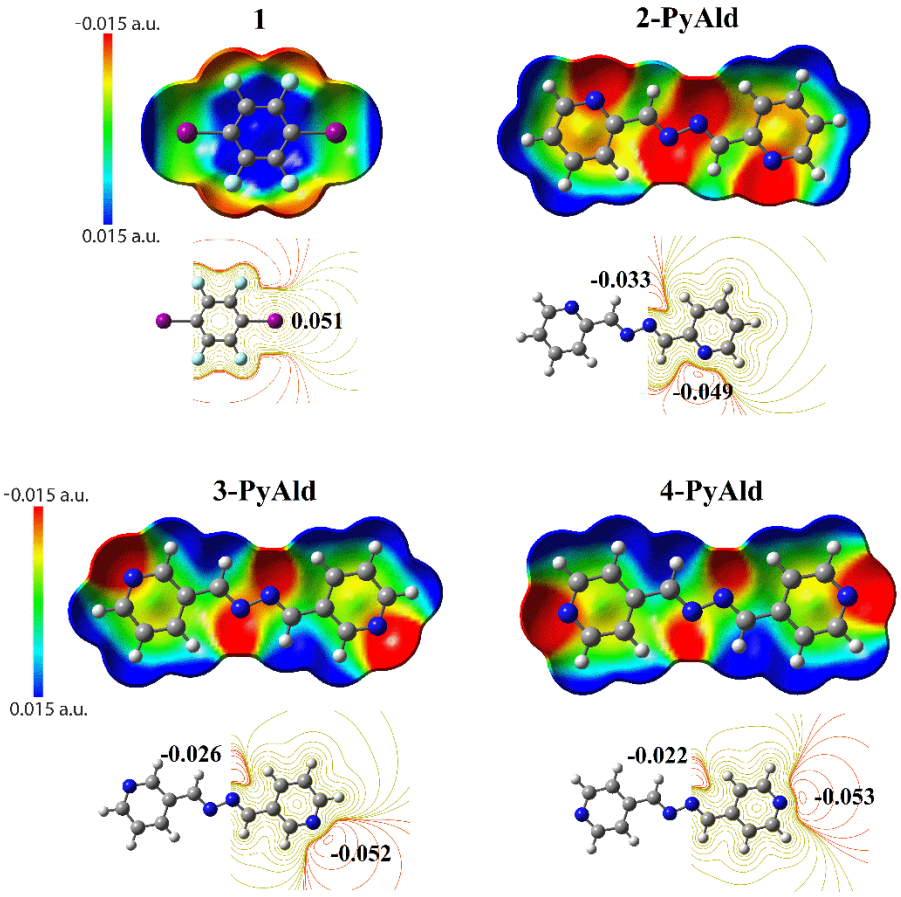

Fig. 10. MEPs for optimised **1** and **n**-PyAld (**n** = 2, 3 and 4) showing charge concentrated (red) and charge depleted (blue) regions. The maximum ($V_{s,max}$; a.u.) and minimum ($V_{s,min}$; a.u.) values of the surface electrostatic potential are indicated in the respective contour plots.

The evaluation of ΔV_s (= $V_{s,max} - V_{s,min}$)[71] for **n**-PyAld in **2–4** suggests the halogen bond strength is in the order **4** > **3** > **2**, as the $V_{s,min}$ values associated with the pyridine-N atoms have an increasing negative potential for the **n** = 2, 3 and 4 isomers, respectively.

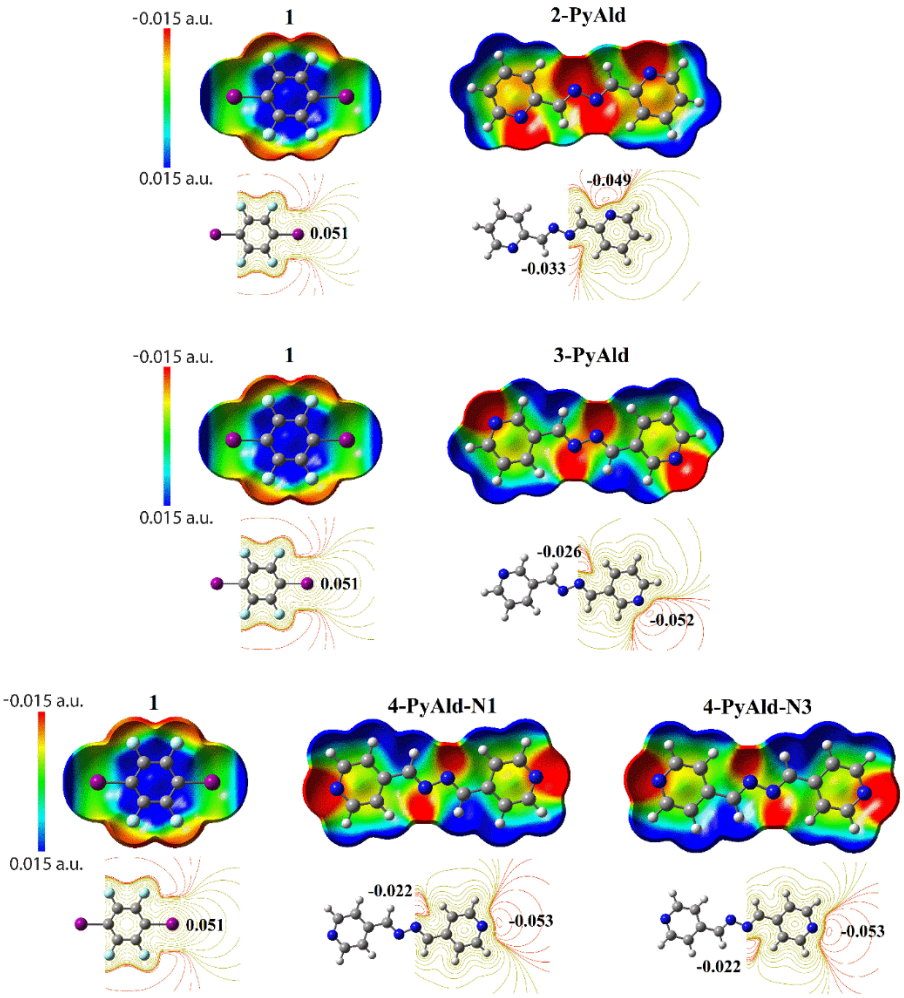

Fig. 11. MEPs for (a) **2**, (b) **3** and (c) **4** showing charge concentrated (red) and charge depleted (blue) regions. The maximum ($V_{s,max}$; a.u.) and minimum ($V_{s,min}$; a.u.) values of the surface electrostatic potential are indicated in the respective contour plots.

Correlations based on electrostatics notwithstanding, the strength of the I···N halogen bonds was further assessed by calculating the interaction energies (ΔE) in **2–4**; Table 5. Single-point calculations performed for **2–4** indicated the most stable interaction is apparent in **3**, *i.e.* -6.3 kcal/mol, being greater than for **4** and then **2** (-5.4 kcal/mol). The obtained energies match those calculated recently for related systems.[72-74] While the present results do not correlate directly with the crystallographic results (Table 2) in terms of I···N separations, it is well known that distance/strength correlations of inherently weak intermolecular interactions are not reliable.[61,75] The results do confirm the potential of regulating the halogen bond strength through the selection of isomeric form of **n**-PyAld.[76]

Vibrational Spectroscopy

The influence of halogen bonding in co-crystals can be readily investigated through vibrational spectroscopy.[77] The FTIR (ESI† Fig. S2) and Raman (ESI† Fig. S3) data for **1–4** are listed in the Experimental section. Notable in the FTIR are red-shifts in the spectra of **2–4** of the bands observed for **1** at 757 cm^{-1}, attributed to ν(C–I),[78-80] and 939 cm^{-1}, ν(C–F),[78-81] as well as ν(C=N)[82] of **n**-PyAz, at ~1630 cm^{-1}, all as a consequence of halogen bond formation.[80,83,84] The theme of small but systematic changes is continued in the evaluation of the solid-state Raman spectra.

Raman spectroscopy is particularly useful for tracking changes in ν(C–X) modes which occur in the range 100–500 cm^{-1}.[20] Perturbations to these are expected upon halogen bonding, such as the manifestation of new bands and/or changes in the intensity.[77] In the Raman

spectrum of **1**, the band observed at 155 cm^{-1} is readily assigned to the symmetric C–I stretch and ring elongation.[78-81,85-86] This undergoes a slight red-shift in **2–4**, with the band intensity greatly reduced.[78,79,86] Co-crystal formation also attenuated the intensity of the active band at 498 cm^{-1}, attributed to the lateral ring expansion along with the ν_s(C–I) and ν_s(C–F) symmetric stretches[78-80,86] in **1**; the frequency remains unchanged. Further, the aryl ring contraction and F-extension band[78-80,86,87] at 1383 cm^{-1} observed in **1** is absent in the Raman spectra of **2–4**. Slight blue-shifts were evident for the bands ascribed to pyridine-ring ν(C–C) and ν(C–N) stretching vibrations[88] when comparing spectra of **n**-PyAld (1568 to 1587 cm^{-1}) with those of corresponding **2**–**4** (1570 to 1588 cm^{-1}).

NMR spectroscopy

NMR spectroscopy is useful in probing halogen bonds through the tracking of changes in the chemical shift for nuclei involved in such interaction.[89-91] In the present study, multinuclear (^{1}H, $^{13}C\{^{1}H\}$, ^{15}N, ^{19}F and ^{127}I) solution state NMR studies for **1**–**4** were performed in 0.1 M $CDCl_3$ solutions despite this solvent is commonly perceived as potentially interacting with solute;[92,93] this choice was dictated by the poor solubility of **2**–**4** in inert solvents such as benzene. Small shifts or no shifts (^{15}N) in the characteristic resonances[38,82,94-96] are noted as indicated in the captions to ESI† Figs S4 to S6.

The $^{13}C\{^{1}H\}$ CPMAS solid-state (SS) NMR spectra for **2**–**4** and **n**-PyAld, and the $^{13}C\{^{1}H\}$ HPDEC MAS SS NMR spectrum of **1** were obtained; those relating to co-crystal **2** are shown in Fig. 12 while those of **3** and **4** are shown in ESI† Fig. S7. A different method was employed for the measurement of $^{13}C\{^{1}H\}$ data for **1** due to the absence of protons in addition to the heavy-atom effect induced by I: this hampered the collection of $^{13}C\{^{1}H\}$ SS NMR spectra with a reasonable signal-to-noise ratio and required long relaxation times.[97] Comparing the solution- and solid-state NMR spectra of **1**–**4** and **n**-PyAld revealed a close

correlation, with the exception of the solid-state spectrum of **4** whereby two ^{13}C signals were resolved for the ortho carbons of the **4**-PyAld coformers. For **1**, the resonances were broad but clearly discernible. In co-crystals **2**–**4**, the ^{13}C resonances attributed to C–I in **2**–**4** are broad, an observation that arises as the I atoms of coformer **1** induce residual dipolar broadening of the ^{13}C signals upon halogen bond formation.[89] As for the solution spectra, the signals due to C–I in **2**–**4** in the solid-state are shifted downfield *cf.* **1**, but by a greater degree *i.e.* 78.4 (**1**) *cf.* 78.9 ppm (Δδ 0.5 ppm), 80.4 ppm (Δδ 2.0 ppm) and 81.8 ppm (Δδ 3.4 ppm) for **2**–**4**, respectively, suggesting the I···N interaction strength in the co-crystals are in the order of **4** > **3** > **2**. The ^{13}C signals due to C–F in **2**–**4** are broad, almost disappearing into the background.

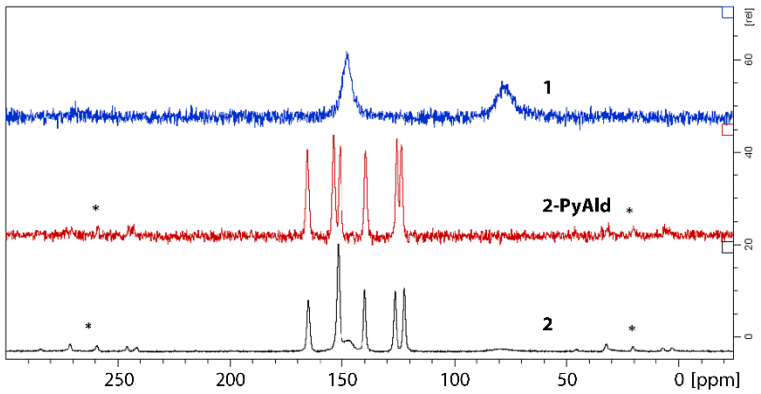

Fig. 12. ^{13}C{^{1}H} SS NMR spectra of **1** (blue trace), **2**-PyAld (red) and **2** (black) measured at 12 kHz. Asterisks denote MAS spinning sidebands.

Solid-state emission Properties

Co-crystallisation of **1** with diverse halogen bond acceptors is a strategic approach to induce phosphorescent emission in co-crystals through the introduction of a heavy-atom perturber.[98] While the luminescence properties of co-crystals constructed from **1** and featuring I···N halogen bonds have been widely explored,[99-107] to the best of our knowledge, the solid-state fluorescence spectrum of **1** has not been reported, largely because heavy atoms *e.g.* I and F, are

effective fluorescence quenchers.[108] The fluorescent features of powders of **2**–**4** were investigated at both room temperature and 77 K. The powders of co-crystals **3** and **4**, and the respective **n**-PyAld coformers are non-emissive at both temperatures. By contrast, the solid-state excitation and emission spectra of **1**, **2**-PyAld and **2** are emissive with the spectra displayed in Fig. 13; **1** is non-emissive at room temperature. Comparing the emission spectra measured at room temperature and 77 K for **1**, **2**-PyAld[109] and **2**, indicates the fluorescent signals are greatly enhanced at the lower temperature. The emission band of **2** at 514 nm recorded at 77 K is comparable to that of **2**-PyAld, indicating that the fluorescent features of **2** can be attributed to $\pi^* \rightarrow \pi$ intra-ligand charge transfer.[109] Interestingly, at 77 K, the broad emission band at λ_{max} 692 nm observed for **1** is not present in the emission spectrum of **2**.

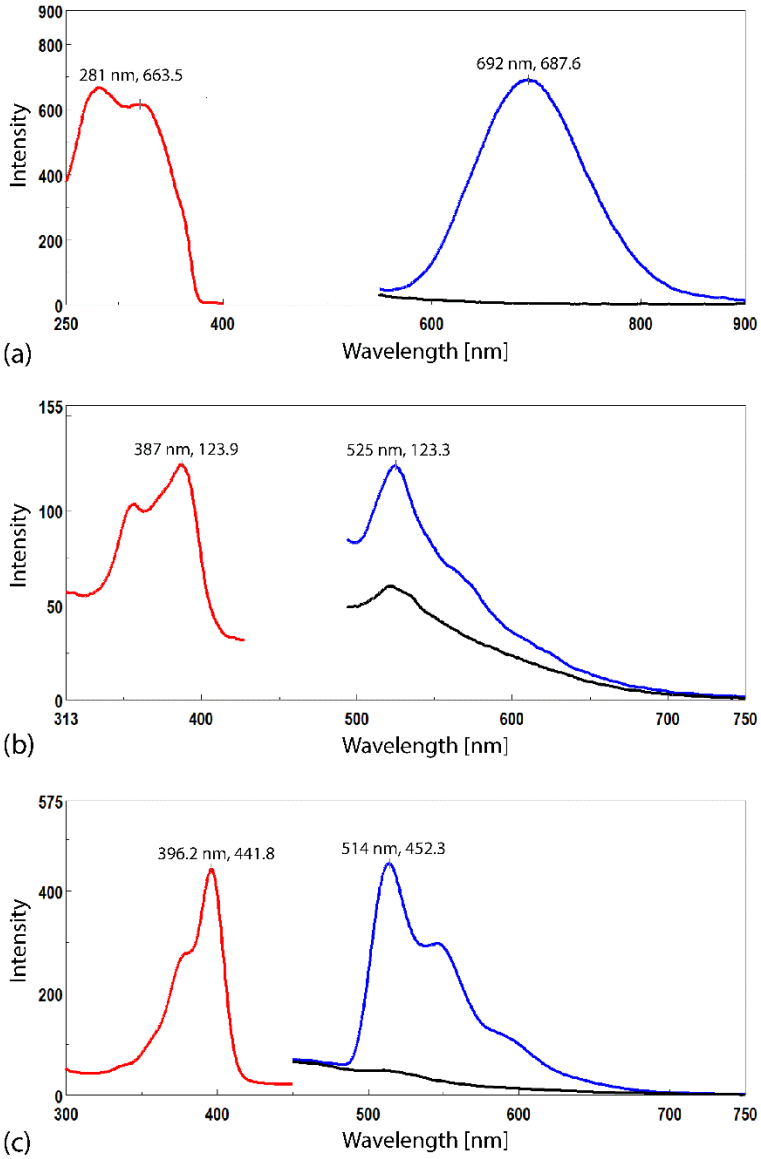

Fig. 13. Solid-state excitation (red trace) and fluorescence emission spectra measured at room temperature (black trace) and 77 K (blue trace) for (a) **1**, (b) **2**-PyAld and (c) **2**; **1** is non-emissive at room temperature.

Intrigued by the absence of the emission band at 692 nm for coformer **1** in the emission spectrum of **2** at 77 K, the fluorescence features of **1** was investigated computationally based on the time dependent (TD) DFT method using Gaussian 09,[45] as per related studies.[110,111] The computed $S_1 \rightarrow S_0$ emission band of **1** (685 nm) is in close agreement with the experimental fluorescent band of **1**. The observed fluorescent properties arise from the charge transfer

originating from the LUMO of I, Fig, 14(a), to the π orbitals *i.e.* HOMO, Fig. 15(b), and *p* orbitals *i.e.* HOMO-3, Fig. 15(c), of **1**. The results rationalise the absence of the emission band at 692 nm in **2**. It is the perturbation of electron distribution in coformer **1** upon co-crystallisation which lowers the occurrence efficiency of the charge transfer process that leads to the quenching of the 692 nm emission band in **2**.

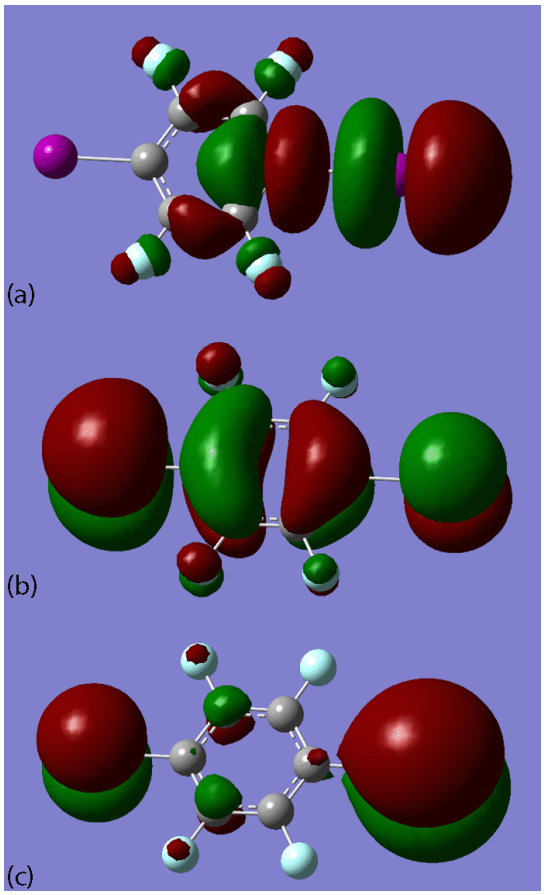

Fig. 14. Images of the (a) LUMO, (b) HOMO and (c) HOMO-3 calculated for **1** at the optimised S_1 state.

Conclusions

Three 1:1 co-crystals of 1,4-diiodotetrafluorobenzene with isomeric **n**-pyridyinealdazines (**n** = 2, 3 and 4) feature I···N halogen bonds within supramolecular chains. The magnitudes of the I···N separations follow the trend **n** = 4 < 3 < 2. The energy of stabilisation provided by the

I···N contacts are small and vary between -5.4 to -6.3 kcal/mol, being a maximum in the crystal with the **n** = 3 isomer. Vibrational spectroscopy confirms the formation of the I···N interactions in the crystals as does solid-state NMR spectroscopy. The induction of distinct topologies correlates with the isomeric form of the **n**-pyridinealdazine coformer and the resultant influence of spectroscopic results, *e.g.* fluorescence, indicates such fine-tuning of properties of co-crystals offer opportunities in materials design.

Author contributions

Chien Ing Yeo: formal analysis, investigation, visualisation, writing – original draft

Yee Seng Tan: formal analysis, investigation, visualisation

Huey Chong Kwong: formal analysis, visualisation, writing – original draft

Vannajan Sanghiran Lee: formal analysis, supervision

Edward R. T. Tiekink: conceptualisation, visualization, writing – original draft

Acknowledgements

The authors gratefully acknowledge Sunway University Sdn Bhd (Grant numbers GRTIN-RRO-08-2022, GRTIN-RRO-12-2022 and GRTIN-RRO-56-2022) for support of this research. Anton Paar Malaysia Sdn Bhd is thanked for providing access to the Anton Paar Cora 5700 Raman instrument.

Conflicts of interest

The authors declare no competing financial interest.

References

1 G. R. Desijaru, P. S. Ho, L. Kloo, A. C. Legon, R. Marquardt, P. Metrangolo, P. Politzer, G. Resnati and K. Rissanen, *Pure Appl. Chem.,* 2013*,* **85***, 1711–1713.*

2 O. Hassel and J. Hvoslef, *Acta Chem. Scand*., 1954, **8**, 873.

3 L. Turunen, J. H. Hansen and M. Erdélyi, *Chem. Rec*., 2021, **21**, 1252–1257

4 M. M. Colin and H. Gaultier de Claubry, *Ann. Chim*., 1814, **90**, 87−100.

5 F. Guthrie, *J. Chem. Soc*., 1863, **16**, 239−244.

6 T. Clark, M. Hennemann, J. S. Murray and P. Politzer, *J. Mol. Model*., 2007, **13**, 291−296.

7 M. H. Kolář and P. Hobza, *Chem. Rev*. 2016, **116**, 5155−5187.

8 P. Politzer and J. S. Murray, *Crystals*, 2017, **7**, 212.

9 N. W. Alcock, *Adv. Inorg. Chem. Radiochem*., 1972, **15**, 1−58.

10 E. R. T. Tiekink, *Coord. Chem. Rev.*, 2021*,* **427**, 213586.

11 E. R. T. Tiekink, *Crystals*, 2021, **11**, 433

12 E. R. T. Tiekink, *Coord. Chem. Rev.*, 2021*,* **443**, 214031.

13 E. R. T. Tiekink, *Coord. Chem. Rev.*, 2022*,* **457**, 214397.

14 H. Wang, W. Wang and W. J. Jin, *Chem. Rev*., 2016, **116**, 5072–5104.

15 S. Scheiner, *J. Phys. Chem. A*, 2021, **125**, 10419–10427.

16 J. P. M. Lommerse, A. J. Stone, R. Taylor and F. H. Allen, *J. Am. Chem. Soc*., 1996, **118**, 3108–3116.

17 E. Corradi, S. V. Meille, M. T. Messina, P. Metrangolo and G. Resnati, *Angew. Chem. Int. Ed*., **2000**, *39*, 1782–1786.

18 P. Metrangolo, H. Neukirch, T. Pilati and G. Resnati, *Acc. Chem. Res*., 2005, **38**, 386–395.

19 A. Mukherjee, S. Tothadi and G. R. Desiraju, *Acc. Chem. Res*., 2014, **47**, 2514–2524.

20 T. Bunchuay, A. Docker, A. J. Martinez-Martinez and P. D. Beer, *Angew. Chem. Int. Ed*., 2019, **58**, 13823–13827.

21 A. Docker, C. H. Guthrie, H. Kuhn and P. D. Beer, *Angew. Chem. Int. Ed*., 2021, **60**, 21973–21978.

22 G. Cavallo, P. Metrangolo, R. Milani, T. Pilati, A. Priimagi, G. Resnati and G. Terraneo, *Chem. Rev*., 2016, **116**, 2478–2601.

23 E. R. T. Tiekink, *Chem. Commun.*, 2014, **50**, 11079–11082.

24 P. Metrangolo, F. Meyer, T. Pilati, D. M. Proserpio and G. Resnati, *Chem. – Eur. J*., 2007, **13**, 5765–5772.

25 K. Raatikainen and K. Rissanen, *CrystEngComm*, 2009, **11**, 750–752.

26 M. A. Sinnwell, J. N. Blad, L. R. Thomas and L. R. MacGillivray, *IUCrJ*, 2018, **5**, 491–496.

27 C. R. Groom, I. J. Bruno, M. P. Lightfoot and S. C. Ward, *Acta Crystallogr., Sect. B: Struct. Sci., Cryst. Eng. Mater*. ,2016, **72**, 171−179.

28 Y. S. Tan, A. Otero-de-la-Roza, M. M. Jotani and E. R. T. Tiekink, *Cryst. Growth Des.*, 2020, **20**, 3272–3283.

29 G. A. Broker, M. M. Jotani and E. R. T. Tiekink, *Acta Crystallogr., Sect. E: Cryst. Commun*., 2017, **73**, 1458–1464.

30 G. A. Broker and E. R. T. Tiekink, *Acta Crystallogr., Sect. E: Struct. Rep. Online*, 2011, **67**, m320–m321.

31 H. D. Arman, P. Poplaukhin and E. R. T. Tiekink, *Acta Crystallogr., Sect. E: Cryst. Commun*., 2016, **72**, 1234–1238.

32 E. R. T. Tiekink, *Crystals*, 2018, **8**, 292.

33 E. R. T. Tiekink, *Crystals*, 2018, **8**, 18.

34 E. R. T. Tiekink, *Coord. Chem. Rev.*, 2017, **345**, 209–228.

35 G. A. Broker, R. P. A. Bettens and E. R. T. Tiekink, *CrystEngComm*, 2008, **10**, 879–887.

36 H. D. Arman, T. Kaulgud, T. Miller and E. R. T. Tiekink, *Z. Kristallogr. Cryst. Mater.*, 2014, **229**, 295–302.

37 B. M. Fung, A. K. Khitrin and K. Ermolaev, *J. Magn. Reson*., 2000, **142**, 97−101.

38 D. A. Edwards, G. M. Hoskins, M. F. Mahon, K. C. Molloy and G. R. G. Rudolph, *Polyhedron*, 1998, **17**, 2321–2326.

39 Rigaku Oxford Diffraction, CrysAlis PRO, Yarnton, Oxfordshire, England (2017).

40 G. M. Sheldrick, *Acta Crystallogr., Sect. A: Found. Crystallogr*., 2008, **64**, 112–122.

41 G. M. Sheldrick, *Acta Crystallogr., Sect. C: Struct. Chem*., 2015, **71**, 3–8.

42 L. J. Farrugia, *J. Appl. Crystallogr*., 2012, **45**, 849–854.

43 A. L. Spek, *Acta Crystallogr., Sect. E: Crystallogr. Commun*., 2020, **76**, 1–11.

44 K. Brandenburg, *DIAMOND*, Crystal Impact GbR, Bonn, Germany, 2006.

45 M. J. Frisch, G. W. Trucks, H. B. Schlegel, G. E. Scuseria, M. A. Robb, J. R. Cheeseman, G. Scalmani, V. Barone, B. Mennucci, G. A. Petersson, H. Nakatsuji, M. Caricato, X. Li, H. P. Hratchian, A. F. Izmaylov, J. Bloino, G. Zheng, J. L. Sonnenberg, M. Hada, M. Ehara, K. Toyota, R. Fukuda, J. Hasegawa, M. Ishida, T. Nakajima, Y. Honda, O. Kitao, H. Nakai, T. Vreven, J. A. Montgomery, Jr., J. E. Peralta, F. Ogliaro, M. Bearpark, J. J. Heyd, E. Brothers, K. N. Kudin, V. N. Staroverov, R. Kobayashi, J. Normand, K. Raghavachari, A. Rendell, J. C. Burant, S. S. Iyengar, J. Tomasi, M. Cossi, N. Rega, J. M. Millam, M. Klene, J. E. Knox, J. B. Cross, V. Bakken, C. Adamo, J. Jaramillo, R. Gomperts, R. E. Stratmann, O. Yazyev, A. J. Austin, R. Cammi, C. Pomelli, J. W. Ochterski, R. L. Martin, K. Morokuma, V. G. Zakrzewski, G. A. Voth, P. Salvador, J. J. Dannenberg, S. Dapprich, A. D. Daniels, Ö. Farkas, J. B. Foresman,

J. V. Ortiz, J. Cioslowski and D. J. Fox. *Gaussian 09, Revision A.1. Gaussian, Inc.*, Wallingford CT, 2009.

46 Y. Zhao and D. G. Truhlar, *Theor. Chem. Acc*., 2008, **120**, 215−241.

47 F. Weigend, M. Häser, H. Patzelt and R. Ahlrichs, *Chem. Phys. Lett.*, 1998, **294**, 143−152.

48 F. Weigend and R. Ahlrichs, *Phys. Chem. Chem. Phys.*, 2005, **7**, 3297−3305.

49 S. Kozuch and J. M. Martin, *J. Chem. Theory Comput*., 2013, **9**, 1918−1931.

50 B. P. Pritchard, D. Altarawy, B. Didier, T. D. Gibson and T. L. Windus, *J. Chem. Inf. Model.*, 2019, **59**, 4814–4820.

51 T. Lu and F. Chen, *J. Mol. Graph. Model*., 2012, **38**, 314–323.

52 S. F. Boys and F. Bernardi, *Mol. Phys.*, 1970, **19**, 553–566.

53 A. D. Becke, *J. Chem. Phys*., 1993, **98**, 5648–5652.

54 C. Lee, W. Yang and R. G. Parr, *Phys. Rev. B*, 1988, **37**, 785–789.

55 B. Miehlich, A. Savin, H. Stoll and H. Preuss, *Chem. Phys. Lett*., 1989, **157**, 200–206.

56 P. Ravat, S. SeethaLekshmi, S. N. Biswas, P. Nandy and S. Varughese, *Cryst. Growth Des*., 2015, **15**, 2389–2401.

57 Y. J. Gao, C. Li, R. Liu and W. J. Jin, *Spectrochim. Acta, Part A*, 2017, **173**, 792–799.

58 R. Wang, D. Hartnick and U. Englert, *Z. Kristallogr. Cryst. Mater*., 2018, **233**, 733–744.

59 F. Otte, J. Kleinheider, W. Hiller, R. Wang, U. Englert and C. Strohmann, *J. Am. Chem. Soc*., 2021, **143**, 4133–4137.

60 E. R. T. Tiekink, *CrystEngComm*, 2021, **23**, 904–928.

61 J. D. Dunitz and R. Taylor, *Chem. – Eur. J*. 1997, **3**, 89–98.

62 K. Reichenbächer, H. I. Süssa and J. Hulliger, *Chem. Soc. Rev*., 2005, **34**, 22–30.

63 J. S. Murray, P. G. Seybold and P. Politzer, *J. Chem. Thermodyn*., 2021, **156**, 106382.

64 J. C. Cole and R. Taylor, *Cryst. Growth Des*., 2022, **22**, 1352–1364.

65 S. K. Wolff, D. J. Grimwood, J. J. McKinnon, M. J. Turner, D. Jayatilaka and M. A. Spackman, Crystal Explorer (Version 17), University of Western Australia, 2012.

66 J. J. McKinnon, M. A. Spackman and A. S. Mitchell, *Acta Crystallogr., Sect. B: Struct. Sci., Cryst. Eng. Mater*., 2004, **60**, 627–668.

67 M. A. Spackman, J. J. McKinnon and D. Jayatilaka, *CrystEngComm*, 2008, **10**, 377–388.

68 L. Happonen, J. M. Rautiainen and A. Valkonen, *Cryst. Growth Des*., 2021, **21**, 3409−3419.

69 N. B. Topić, N. Bedeković, K. Lisac, V. Stilinović and D. Cinčić, *Cryst. Growth Des.*, 2022, **22**, 3981–3989.

70 R. Bhowal, S. Biswas, D. P. A. Saseendran, A. L. Koner and D. Chopra, *CrystEngComm*, 2019, **21**, 1940–1947.

71 D. Musumeci, C. A. Hunter, R. Prohens, S. Scuderi and J. F. McCabe, ***Chem. Sci.***, 2011, **2**, 883–890.

72 Y. V. Torubaev and I. V. Skabitsky, *CrystEngComm*, 2019, **21**, 7057−7068.

73 I. G. Grosu, L. Pop, M. Miclăuş, N. D. Hădade, A. Terec, A. Bende, C. Socaci, M. Barboiu and I. Grosu, *Cryst. Growth Des*., 2020, **20**, 3429−3441.

74 L. Pop, I. G. Grosu, M. Miclăuş, N. D. Hădade, A. Pop, A. Bende, A. Terec, M. Barboiu and I. Grosu, *Cryst. Growth Des*., 2021, **21**, 1045−1054.

75 E. R. T. Tiekink and J. Zukerman-Schpector, *CrystEngComm*, 2009, **11**, 2701–2711.

76 K. E. Riley, J. S. Murray, J. Fanfrlík, J. Řezáč, R. J. Solá, M. C. Concha, F. M. Ramos, and P. Politzer, *J. Mol. Model*., 2011, **17**, 3309–3318.

77 M. Erdélyi, *Chem. Soc. Rev*., 2012, **41**, 3547–3557.

78 G. R. Hanson, P. Jensen, J. McMurtrie, L. Rintoul and A. S. Micallef, *Chem. – Eur. J.*, 2009, **15**, 4156–4164.

79 Q. J. Shen, X. Pang, X. R. Zhao, H. Y. Gao, H.-J. Sun and W. J. Jin, *CrystEngComm*, 2012, **14**, 5027–5034.

80 H. Wang and W. J. Jin, *Acta Crystallogr., Sect. B: Struct. Sci., Cryst. Eng. Mater.*, 2017, **73**, 210–216.

81 X. Pang, X. R. Zhao, H. Wang, H.-L. Sun and W. J. Jin, *Cryst. Growth Des.*, 2013, **13**, 3739−3745.

82 D. Sek, M. Siwy, K. Bijak, M. Grucela-Zajac, G. Malecki, K. Smolarek, L. Bujak, S. Mackowski and E. Schab-Balcerzak, *J. Phys. Chem. A*, 2013, **117**, 10320−10332.

83 B. A. DeHaven, A. L. Chen, E. A. Shimizu, S. R. Salpage, M. D. Smith and L. S. Shimizu, *Supramol. Chem.*, 2018, **30**, 315–327.

84 R. A. Wiscons and A. J. Matzger, *Cryst. Growth Des*., 2017, **17**, 901–906.

85 S. d'Agostino, F. Spinelli, P. Taddei, B. Ventura and F. Grepioni, *Cryst. Growth Des.*, 2019, **19**, 336−346.

86 H. Y. Gao, Q. J. Shen, X. R. Zhao, X. Q. Yan, X. Pang and W. J. Jin, *J. Mater. Chem.*, 2012, **22**, 5336–5343.

87 H. Y. Gao, X. R. Zhao, H. Wang, X. Pang and W. J. Jin, *Cryst. Growth Des.*, 2012, **12**, 4377−4387.

88 M. Pižl, A. Picchiotti, M. Rebarz, N. Lenngren, L. Yingliang, S. Záliš, M. Kloz and A. Vlček, *J. Phys. Chem. A*, 2020, **124**, 1253−1265.

89 J. Viger-Gravel and D. L. Bryce, *Top Curr. Chem*., 2015, **358**, 183–204.

90 D. von der Heiden, A. Vanderkoov and M. Erdélyi, *Coord. Chem. Rev.*, 2020, **407**, 213147.

91 B. Jimmink, D. Sethio, L. Turunen, D. von der Heiden and M. Erdélyi, *J. Am. Chem. Soc*., 2021, **143**, 10695–10699.

92 B. Hawthorne, H. Fan-Hagenstein, E. Wood, J. Smith and T. Hanks, *Int. J. Spectrosc*., 2013, 216518.

93 M. G. Sarwar, B. Dragisic, L. J. Salsberg, C. Gouliaras and M. S. Taylor, *J. Am. Chem. Soc*., 2010, **132**, 1646–1653.

94 S. Verma, V. Vajpayee, S. M. Lee, H. J. Jung, H. Kim, and K.-W. Chi, *Inorg. Chim. Acta*, 2012, **387**, 435–440.

95 R. Arulmani, R. Balachander, P. Vijaya and K. R. Sankaran, *Spectrochim. Acta A Mol. Biomol. Spectrosc*., 2015, **138**, 660–666.

96 Z. R. Ranjbar, A. Morsali and P. Retailleau, *Inorg. Chim. Acta*, 2011, 376, 486–491.

97 J. Viger-Gravel, S. Leclerc, I. Korobkov and D. L. Bryce, *CrystEngComm*, 2013, **15**, 3168–3177.

98 X.-H. Ding, Y.-Z.; Chang, C.-J. Ou, J.-Y. Lin, L.-H. Xie and W. Huang, *Natl. Sci. Rev*., 2020, **7**, 1906–1932.

99 L. Bai, P. Bose, Q. Gao, Y. Li, R. Ganguly and Y. Zhao, *J. Am. Chem. Soc*., 2017, **139**, 436–441.

100 E. Lucenti, A. Forni, C. Botta, C. Giannini, D. Malpicci, D. Marinotto, A. Previtali, S. Righetto and E. Cariati, *Chem. – Eur. J*., 2019, **25**, 2452–2456.

101 A. Li, J. Wang, Y. Liu, S. Xu, N. Chu, Y. Geng, B. Li, B. Xu, H. Cui and W. Xu, *Phys. Chem. Chem. Phys*., 2018, **20**, 30297–30303.

102 A. O. Weldeab, A. Steen, D. J. Starkenburg, J. S. D. Williams, K. A. Abboud, J. Xue, N. I. Hammer, R. K. Castellano and D. L. Watkins, *J. Mater. Chem. C*, 2018, **6**, 11992–12000.

103 F. Grepioni, S. d'Agostino, D. Braga, A. Bertocco, L. Catalano and B. Ventura, *J. Mater. Chem. C*, 2015, **3**, 9425–9434.

104 H. Lin, X. Chang, D. Yan, W.-H. Fang and G. Cui, *Chem. Sci*., 2017, **8**, 2086–2090.

105 D. Yan, A. Delori, G. O. Lluoyd, T. Friščić, G. M. Day, W. Jones, J. Lu, M. Wei, D. G. Evans and X. Duan, *Angew. Chem. Int. Ed*., 2011, **50**, 12483–12486.

106 C. Feng, S. Li, X. Xiao, Y. Lei, H. Geng, Y. Liao, Q. Liao, J. Yao, Y. Wu and H.; Fu, *Adv. Optical Mater*., 2019, **7**, 1900767.

107 A. Li, J. He, J. Wang, C. Bi, S. Xu, W. Xu and H.; Cui, *Dyes Pigm*., 2020, **175**, 108116.

108 M. N. Berberan-Santos, *PhysChemComm*, 2000, **3**, 18–23.

109 Y. Bai, G.-Q. Zhang, D.-B. Dang, P.-T. Ma, H. Gao and J.-Y. Niu, *CrystEngComm*, 2011, **13**, 4181–4187.

110 P. Yu, Y. Li Y. Zhen, H. Dong and W. Hu, Tailoring the strength and number of halogen bonds toward room temperature phosphorescent micro-cocrystals. *Nano Select*., 2021, **2**, 1509–1516.

111 G. R. Morello, Accurate prediction of emission energies with TD-DFT methods for platinum and iridium OLED materials. *J. Mol. Model*., 2017, **23**, 174.